Speckle-correlation imaging through a kaleidoscopic multimode fiber

Dorian Bouchet, Antonio Miguel Caravaca-Aguirre, Guillaume Godefroy, Philippe Moreau, Irène Wang, Emmanuel Bossy

PNAS RESEARCH ARTICLE | APPLIED PHYSICAL SCIENCES

Speckle-correlation imaging through a kaleidoscopic multimode fiber

Dorian Bouchet[a,1], Antonio Miguel Caravaca-Aguirre[a], Guillaume Godefroy[a,b], Philippe Moreau[a], Irène Wang[a], and Emmanuel Bossy[a]

Edited by Hui Cao, Yale University, New Haven, CT; received December 17, 2022; accepted May 23, 2023

Speckle-correlation imaging techniques are widely used for noninvasive imaging through complex scattering media. While light propagation through multimode fibers and scattering media share many analogies, reconstructing images through multimode fibers from speckle correlations remains an unsolved challenge. Here, we exploit a kaleidoscopic memory effect emerging in square-core multimode fibers and demonstrate fluorescence imaging with no prior knowledge on the fiber. Experimentally, our approach simply requires to translate random speckle patterns at the input of a square-core fiber and to measure the resulting fluorescence intensity with a bucket detector. The image of the fluorescent object is then reconstructed from the autocorrelation of the measured signal by solving an inverse problem. This strategy does not require the knowledge of the fragile deterministic relation between input and output fields, which makes it promising for the development of flexible minimally invasive endoscopes.

light propagation | optical imaging | multimode fibers | speckle correlations | memory effect

Significance

By reflecting light multiple times, a simple object seen through a kaleidoscope transforms into a beautiful, complex symmetrical pattern. Here, we show that this effect can actually be used the other way around to unscramble the complexity of light propagation in multimode fibers and transform highly complex measured patterns into clear images. Indeed, in usual circular-core multimode fibers, light is strongly scrambled, in the same way as in disordered scattering media. This is also true for square-core multimode fibers, but thanks to the kaleidoscopic effect, we were able to reconstruct images of fluorescent objects through the fiber without any prior knowledge about the fiber.

The development of optical endoscopes is motivated by a number of biomedical applications such as brain imaging (1). Multimode fibers are excellent candidates to minimize the invasiveness of such procedures, as they feature a high density of modes per unit area (2, 3). However, coherent light propagating inside such fibers typically generates speckle patterns at the fiber output, in a similar way as through complex scattering media (4). Different methods have emerged to exploit the complex deterministic relation between incident and transmitted fields in multimode fibers, based on either experimental measurements (5–11) or theoretical modeling (12, 13). Nevertheless, these methods require either an optical access to both sides of the fiber or a precise knowledge of the fiber geometry over its entire length, which makes them unsuitable for many applications.

In contrast, statistical approaches based on speckle correlations can be implemented without such prior information. In the last decade, these strategies have been successfully employed to image fluorescent objects through layers of scattering materials (14–18). A key component of these approaches is the existence of a memory effect, which creates statistical correlations between incident and transmitted fields (19–24). However, multimode fibers have different statistical properties as compared to scattering materials (25–27). A rotational memory effect exists in commonly used circular-core multimode fibers (25), but it must be completed by additional information (using, e.g., a fluorescent guidestar) in order to form an image (27). Recently, deep neural networks have emerged as promising tools to learn not only deterministic but also statistical relations in multimode fibers (28–31), but with a generalizability limited to the specific experimental conditions under which the training dataset was measured. Thus, most practical implementations of fiber-optic endoscopes remain currently based on multicore fibers (32–34), which are characterized by a much larger footprint as compared to multimode fibers.

Traditionally, in optical fibers, the geometry of the core is circular, and the use of square-core fibers is limited to specific applications requiring a top-hat-like intensity profile (35). However, it was recently observed that a kaleidoscopic memory effect emerges from the strong symmetry properties of square-core multimode fibers (36). This effect is a special type of shift–shift correlation (23): any pattern translating at the fiber input leads to speckle patterns shifting along four directions at the output. The memory effect thus spans the whole two-dimensional (2D) space in square-core fibers, as opposed to conventional multimode fibers with a circular core geometry for which there exists no true radially shifting memory effect (25, 27). Taking advantage of the kaleidoscopic memory effect in square-core fibers, we present here a fully statistical method to perform endoscopic imaging from speckle correlations, without relying on transmission matrix measurements or on fluorescent guidestars.

Author affiliations: [a]Université Grenoble Alpes, CNRS, LIPhy, 38000 Grenoble, France; and [b]Université Grenoble Alpes, CEA, Leti, 38000 Grenoble, France

Author contributions: D.B., I.W., and E.B. designed research; D.B., A.M.C.-A., G.G., P.M., I.W., and E.B. performed research; D.B. and E.B. analyzed data; and D.B. and E.B. wrote the paper.

Competing interest statement: A.M.C.-A. is currently an employee of Modendo Inc., a startup company. A.M.C.-A and E.B. have a patent relevant to speckle-correlation imaging through square-core multimode fibers.

This article is a PNAS Direct Submission.

[1]To whom correspondence may be addressed. Email: dorian.bouchet@univ-grenoble-alpes.fr.

This article contains supporting information online at https://www.pnas.org/lookup/suppl/doi:10.1073/pnas.2221407120/-/DCSupplemental.

Published June 21, 2023.

Principle

The principle of the proposed approach is illustrated in Fig. 1 (see also *Materials and Methods* for a detailed description of the experimental setup). A fluorescent sample is placed at the output of a step-index square-core optical fiber (CeramOptec, core section 100 μm × 100 μm). In our proof-of-principle experiment, this sample is composed of several fluorescent beads (ThermoFisher Scientific, red FluoSpheres, diameter 1.0 μm). We generate random speckle patterns at the fiber input using a digital micromirror device (DMD), and the transmitted light forms unknown speckle patterns that excite the fluorescent beads. Fluorescence collected through the fiber is then measured by a bucket detector located at the fiber input.

In order to exploit shift–shift correlations in the fiber, we translate the incident field in the transverse plane, and we measure the resulting fluorescence signal $S(\boldsymbol{r}_a)$, with a scan area of 8 μm × 8 μm. While this signal visually appears as being random, it does carry useful information about the hidden fluorescent object. More precisely, the density distribution of fluorescent emitters $O(\boldsymbol{r}_b)$ is related to the measured fluorescence signal $S(\boldsymbol{r}_a)$ by the following relation:

$$S(\boldsymbol{r}_a) = \int O(\boldsymbol{r}_b) I(\boldsymbol{r}_a, \boldsymbol{r}_b)\, \mathrm{d}\boldsymbol{r}_b\,, \qquad [1]$$

where $I(\boldsymbol{r}_a, \boldsymbol{r}_b)$ is the (unknown) excitation intensity transmitted at a position $\boldsymbol{r}_b$ at the fiber output for a translation $\boldsymbol{r}_a$ of the speckle pattern at the fiber input. From Eq. **1**, we demonstrate in *SI Appendix*, section 2A, that the normalized autocorrelation function of the measured fluorescence signal is expressed as follows (see also Fig. 2 for a graphical interpretation of this equation):

$$C_S(\Delta\boldsymbol{r}_a) = K^{-2} \int C_O(\Delta\boldsymbol{r}_b) C_I(\Delta\boldsymbol{r}_a, \Delta\boldsymbol{r}_b)\, \mathrm{d}\Delta\boldsymbol{r}_b\,, \qquad [2]$$

where $C_O(\Delta\boldsymbol{r}_b)$ is the autocorrelation of the fluorescent object, $C_I(\Delta\boldsymbol{r}_a, \Delta\boldsymbol{r}_b)$ is the (known) intensity correlation function of the transmitted excitation intensity, and K is a normalization constant equal to the contrast of the fluorescence signal. In our work, C_I is known from experimental measurements (*SI Appendix*, section 3).

Eq. **2**, which does not directly involve the object but its autocorrelation (Fig. 2 *B* and *C*), is formally identical to the one describing how to image fluorescent objects through scattering layers (14). However, while the intensity correlation function C_I describing light propagation through scattering layers is characterized by a single peak arising from the usual memory effect (19, 20), the symmetry of the fiber generates a kaleidoscopic memory effect characterized by a different intensity correlation function (36). Indeed, C_I is then characterized by four peaks that translate with $\Delta\boldsymbol{r}_a$ and that coherently overlap by pair when $\Delta x_a = 0$ or $\Delta y_a = 0$ (Fig. 2 *D*–*G*). As a consequence, the autocorrelation of the measured fluorescence signal does not directly yield the object autocorrelation. Instead, it involves $C_O^{\mathrm{sym}}(\Delta\boldsymbol{r}_b) = [C_O(\Delta x_b, \Delta y_b) + C_O(\Delta x_b, -\Delta y_b)]/2$, which is a symmetrized version of the object autocorrelation: indeed, since C_O is centrosymmetric, one gets $C_O^{\mathrm{sym}}(-\Delta x_b, \Delta y_b) = C_O^{\mathrm{sym}}(\Delta x_b, \Delta y_b)$ and $C_O^{\mathrm{sym}}(\Delta x_b, -\Delta y_b) = C_O^{\mathrm{sym}}(\Delta x_b, \Delta y_b)$, as illustrated by Fig. 2*H*.

In order to understand how the signal autocorrelation C_S relates to the symmetrized object autocorrelation C_O^{sym}, it is instructive to first consider the limiting case of an infinite-range memory effect with a speckle grain size approaching zero. In this case, Eq. **2** yields $C_S(\Delta\boldsymbol{r}_a) \propto w(\Delta\boldsymbol{r}_a) C_O^{\mathrm{sym}}(\Delta\boldsymbol{r}_a)$, where w is a weight function that is equal to 1 if $\Delta x_a = 0$ and $\Delta y_a = 0$, to 1/2 if either $\Delta x_a = 0$ or $\Delta y_a = 0$, and to 1/4 otherwise (*SI Appendix*, section 2B). In practice, the translational memory effect observed in typical step-index square-core optical fibers is further characterized by a limited range (36), and the measured intensity correlation $C_I(\Delta\boldsymbol{r}_a, \Delta\boldsymbol{r}_b)$ gradually decays with the distance $\Delta\boldsymbol{r}_a$. As a consequence, the signal autocorrelation $C_S(\Delta\boldsymbol{r}_a)$ predicted from Eq. **2** also decays with $\Delta\boldsymbol{r}_a$ (Fig. 2*I*), limiting the potential reconstruction area to approximately 10 μm × 10 μm for the type of step-index fiber used in our experiment. In addition, the finite size of the speckle grain limits the achievable resolution of the method, which is of approximately 1.2 μm in our experiment (excitation wavelength $\lambda = 532$ nm; fiber numerical aperture NA = 0.22).

Reconstructing fluorescent objects from measurements of the signal autocorrelation C_S thus amounts to retrieve O from C_O^{sym}. This inverse problem has no known explicit solution, but it can be solved iteratively by exploiting additional prior knowledge about the object as constraints. This problem is in fact deeply connected to commonly encountered phase-retrieval problems (37, 38), and especially to autocorrelation inversions (14). It essentially differs from such problems in two aspects. First, as the intensity correlation function $C_I(\Delta\boldsymbol{r}_a, \Delta\boldsymbol{r}_b)$ is characterized by four peaks instead of one, there exists an additional ambiguity in the inverse problem to be solved. Indeed,

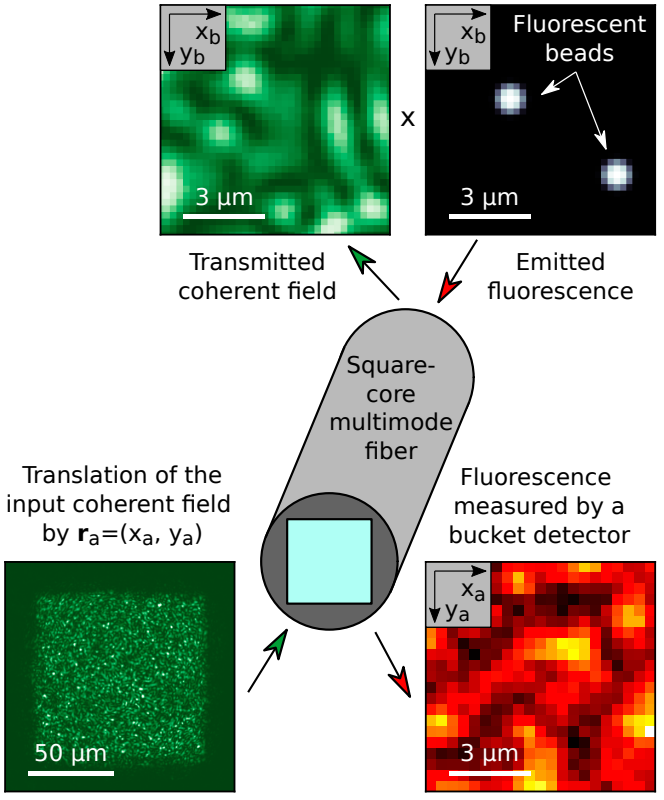

Fig. 1. Principle of a minimally invasive endoscope based on a square-core multimode fiber. Coherent speckle patterns are translated in the transverse plane at the input of a square-core multimode fiber. Transmitted intensity patterns, which are unknown, excite a fluorescent sample located at the output of the fiber. Fluorescence is collected by the same fiber and is subsequently measured by a bucket detector located at the fiber input. Our method enables one to reconstruct an image of the sample from the seemingly random fluorescence signal measured as a function of the translation $\boldsymbol{r}_a$ of the input field.

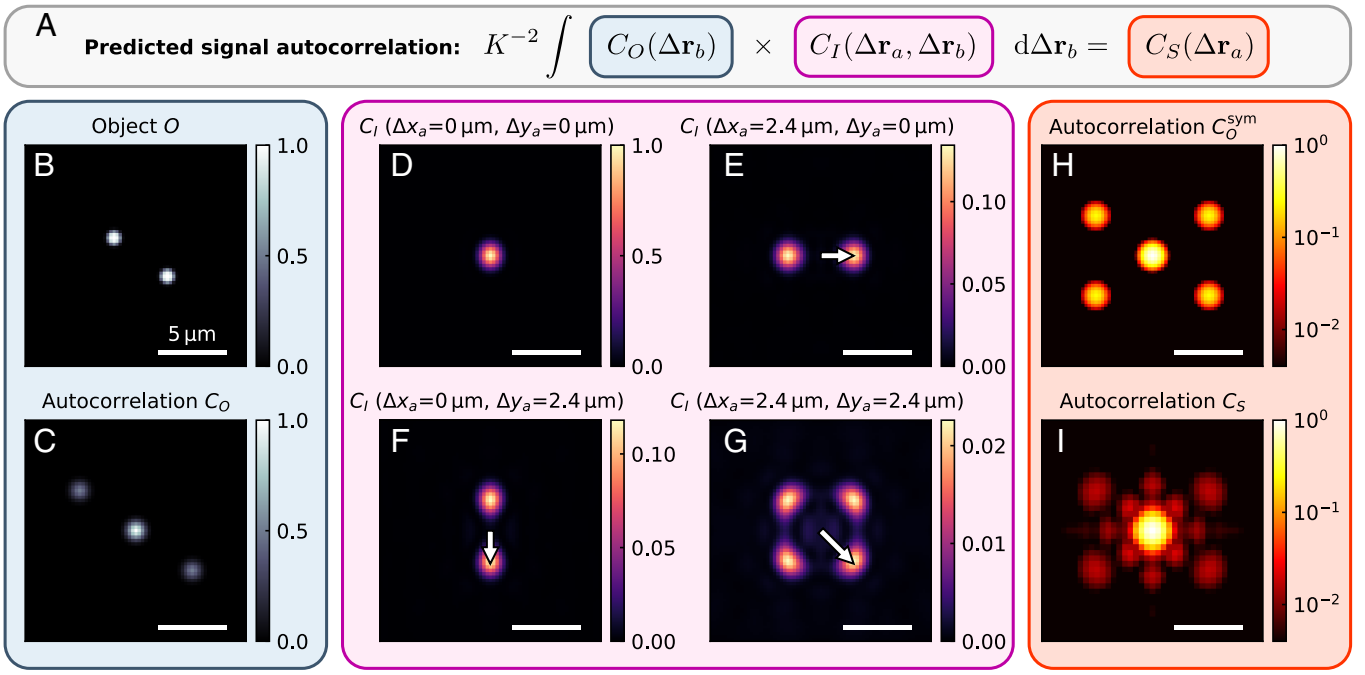

Fig. 2. Predicted autocorrelation of the fluorescence signal. (*A*) Graphical representation of Eq. **2** relating the object autocorrelation $C_O(\Delta\boldsymbol{r}_b)$, the intensity correlation function of the excitation field $C_I(\Delta\boldsymbol{r}_a, \Delta\boldsymbol{r}_b)$, and the autocorrelation of the fluorescence signal $C_S(\Delta\boldsymbol{r}_a)$. (*B*) Fluorescent object $O(\boldsymbol{r}_b)$ composed of two beads (diameter, 1.0 µm), that we model here using high-order Gaussian functions. (*C*) Object autocorrelation $C_O(\Delta\boldsymbol{r}_b)$ calculated from $O(\boldsymbol{r}_b)$. (*D*–*G*) Intensity correlation function of the excitation field $C_I(\Delta\boldsymbol{r}_a, \Delta\boldsymbol{r}_b)$, represented as a function of $\Delta\boldsymbol{r}_b$ (shift at the fiber output) for four different values of $\Delta\boldsymbol{r}_a$ (shift at the fiber input). This correlation function, which characterizes light propagation in square-core multimode fibers, is composed of four peaks that translate when changing the value of $\Delta\boldsymbol{r}_a$ (white arrows on the figures). (*H*) Symmetrized autocorrelation of the object $C_O^{\mathrm{sym}}(\Delta\boldsymbol{r}_b)$. (*I*) Predicted signal autocorrelation $C_S(\Delta\boldsymbol{r}_a)$ calculated using Eq. **2**. The four main lobes that appear in $C_O^{\mathrm{sym}}(\Delta\boldsymbol{r}_b)$ are also identified in $C_S(\Delta\boldsymbol{r}_a)$, but with a smaller amplitude due to the finite range of the memory effect. A number of additional lobes can be identified close to the central peak due to the presence of lobes in the intensity correlation function $C_I(\Delta\boldsymbol{r}_a, \Delta\boldsymbol{r}_b)$.

for a given fluorescent object, there exist four equivalent solutions that are flipped versions of the object (*SI Appendix*, section 4), instead of two in typical autocorrelation inversions. Second, the signal autocorrelation is weighted by a factor of 1/4 (instead of 1) when $\Delta x_a \neq 0$ and $\Delta y_a \neq 0$. This effect, when cumulated to the continuous decay of the correlation function with $\Delta\boldsymbol{r}_a$, increases the influence of the statistical fluctuations that are observed when estimating correlation functions from experimental measurements. In practice, to counteract this effect, we generate and translate random incident fields at kHz framerate using the DMD; this allows us to average the signal correlation function over many random configurations of the input speckle, thereby minimizing the apparition of artifacts due to statistical fluctuations.

Experimental Results

Imaging through a Static Fiber. We first experimentally illustrate this approach with a static fiber (fiber length 3 cm), that we used to successively probe three different fluorescent objects (Fig. 3 *A*–*C*). The predicted signal autocorrelation function (Fig. 3 *D*–*F*), calculated using Eq. **2**, strongly depends on the object, which explicitly demonstrates that this function does carry spatial information about the object. Moreover, autocorrelation functions retrieved from experimental measurements (Fig. 3 *G*–*I*) are in excellent agreement with theoretically predicted ones. These results were obtained by averaging over $N_{\mathrm{rep}} = 40{,}000$ realizations of input speckles; while reducing N_{rep} inevitably leads to the apparition of artifacts due to statistical fluctuations, some spatial information about the fluorescent objects is still present even for much lower values of N_{rep} (*SI Appendix*, section 5). Based on these experimental data and on the forward model expressed by Eq. **2**, we could in principle reconstruct an image using a pixel-by-pixel approach. However, the inverse problem is more easily solved when using additional a priori information about the object. Here, we take advantage of known characteristics of the beads, setting a bead diameter of 1 µm and assuming that all beads have the same brightness. We then estimate the number of fluorescent beads using the statistics of the measured signal (*SI Appendix*, section 6). Finally, we used an optimization algorithm based on simulated annealing (39) in order to find the position of the beads that minimize the error between theoretical predictions and experimental data (*SI Appendix*, section 7). The reconstructed images (Fig. 3 *J*–*L*) are in excellent agreement with direct images of the objects (i.e., the ground truths), demonstrating that even though light is apparently scrambled when propagating through square-core multimode fibers, 2D spatial information about fluorescent objects can be effectively recovered with a fully statistical imaging strategy.

Imaging through a Dynamically Perturbed Fiber. Endoscopic imaging techniques based on transmission matrix measurements are known to be very sensitive to external perturbations such as vibrations and fiber bending. In contrast, our approach based on speckle correlations is intrinsically robust to such perturbations. To experimentally demonstrate this crucial advantage, we used a 10.5-cm-long fiber, which can be more easily deformed as compared to the 3-cm-long fiber. To ensure that this longer fiber length does not affect the efficiency of the method, we can compare the intensity correlation function $C_I(\Delta\boldsymbol{r}_a, \Delta\boldsymbol{r}_b)$

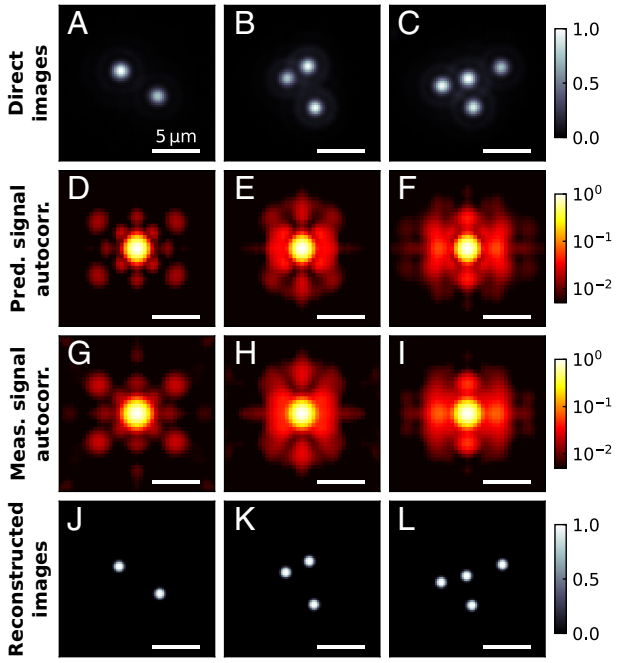

Fig. 3. Reconstructed images of fluorescent beads through a square-core fiber. (*A–C*) Direct fluorescence images of objects composed of several fluorescent beads, that are located at the output of a 3-cm-long fiber. (*D–F*) Predicted signal autocorrelations calculated with the true position of the beads using Eq. **2**. (*G–I*) Signal autocorrelations retrieved from experimental measurements (averaged over $N_{\text{rep}} = 40{,}000$ speckle illuminations). (*J–L*) Reconstructed images of the beads. The number of beads is first estimated independently from the statistics of the measured signal (*SI Appendix*, section 6), and the position of the beads is then retrieved using an optimization algorithm based on simulated annealing.

measured for the 3-cm-long fiber and for the 10.5-cm-long fiber. These two correlation functions are very similar (*SI Appendix*, section 3), evidencing that the kaleidoscopic memory effect is robust in this range of fiber lengths.

To verify that our approach is robust to external perturbations, we deformed the fiber by pushing it at midlength using a rod controlled by a motorized stage (Fig. 4 *A* and *B*). Such a perturbation strongly modifies the propagation of light through the fiber, as can be verified by generating a random speckle pattern at the fiber input and by measuring output speckle patterns for different displacements δ of the rod. Speckle patterns measured for $\delta = 0\,\mu$m and $\delta = 100\,\mu$m are strongly different (Fig. 4 *C* and *D*) due to a decorrelation of the measured patterns as well as to a transverse shift of the fiber (*SI Appendix*, section 8). To quantitatively analyze this perturbation, we calculated the correlation coefficient of the speckle patterns as a function of the displacement δ, taking as a reference the speckle pattern measured for $\delta = 0\,\mu$m. The value of the correlation coefficient decreases from one to zero for a displacement of the rod of approximately 20 μm (Fig. 4*E*), evidencing that the transmission matrix of the imaging system is completely modified by a displacement $\delta \geq 20\,\mu$m. In contrast, the intensity correlation function $C_I(\Delta \boldsymbol{r}_a, \Delta \boldsymbol{r}_b)$ remains identical before and after a displacement of 100 μm (*SI Appendix*, section 3), which demonstrates the robustness of the kaleidoscopic memory effect to such perturbations.

In our experiments, to reproduce the dynamical aspect of the perturbations that typically occur when studying living organisms, we continuously modified the position of the rod perturbing the fiber by applying a periodic displacement over a range of 100 μm (Fig. 4*F*). We show in Movie S1 the decorrelation of the speckle patterns induced by this periodic displacement of the rod. While the time period of the perturbation (6 s) is much shorter than the total acquisition time (approximately 4 h), this does not affect the efficiency of our approach. Indeed, some stability is required when scanning a given input speckle pattern (220 ms in our experiments), but the system may be perturbed between two different random realizations of the input speckle pattern.

We used this dynamically perturbed fiber to successively study two different objects, each composed of four fluorescent beads (Fig. 4 *G* and *H*). The predicted signal autocorrelations (Fig. 4 *I* and *J*) are again in excellent agreement with the measured signal autocorrelations (Fig. 4 *K* and *L*), and images are faithfully reconstructed by the reconstruction algorithm (Fig. 4 *K* and *L*). Note that similar results were also obtained by maintaining the fiber in a static position (*SI Appendix*, section 9), which confirms that the dynamical aspect of the applied perturbation does not significantly influence the efficiency of the method. As such, these results explicitly demonstrate that our approach is robust to fiber perturbations, far beyond what is achievable with transmission matrix measurements.

Discussion

To further investigate the possibility to image more complicated objects using the same approach, we performed a complementary study based on numerical simulations. For this purpose, we used as objects grayscale images from the MNIST database of handwritten digits (Fig. 5 *A–C*). Using Eq. **2**, we then numerically generated the associated signal autocorrelations (Fig. 5 *D–F*), based on the intensity correlation function $C_I(\Delta \boldsymbol{r}_a, \Delta \boldsymbol{r}_b)$ that was measured in the experiment. This constitutes a direct approach to model the signal autocorrelations that would be measured with our optical setup, taking into account the finite numerical aperture of the fiber and the limited range of the memory effect, but however without describing the influence of statistical fluctuations. We then trained two different artificial neural networks in parallel to solve the inverse problem from these signal autocorrelations (*Materials and Methods*), one for classification [a DenseNet (40)] and one for image reconstruction [a UNeXt (41)]. Testing these neural networks on unseen objects, we obtain a classification accuracy of 91% using the DenseNet, and images are reconstructed with a high fidelity by the UNeXt (Fig. 5 *G–I*, see also *SI Appendix*, section 10), with an average structural similarity between ground truths and reconstructed images of 0.89. This demonstrates that the inverse problem underlying our approach can be successfully solved not only in the case of a few point-like objects but also in the case of more complicated, continuous objects.

For many applications, the acquisition time is an important parameter that should be minimized. While the acquisition time was approximately 4 h in our proof-of-principle experiments, there exist several opportunities to increase the speed of such measurements. For instance, in our work, input fields are translated with a step size of 0.4 μm, while the resolution limit of the system is $\lambda/(2\text{NA}) \simeq 1.2\,\mu$m; one could thus use a larger step size without impacting the resolution of reconstructed images. Other ideas could also be implemented to reduce the acquisition time, such as working with a more sensitive photomultiplier, brighter fluorescent beads, and a DMD with a larger on-board memory (*Materials and Methods*). In addition, the number of different input fields needed to reconstruct the objects could also be strongly decreased. Indeed, while we worked with 40,000 realizations to minimize the apparition of fluctuation-

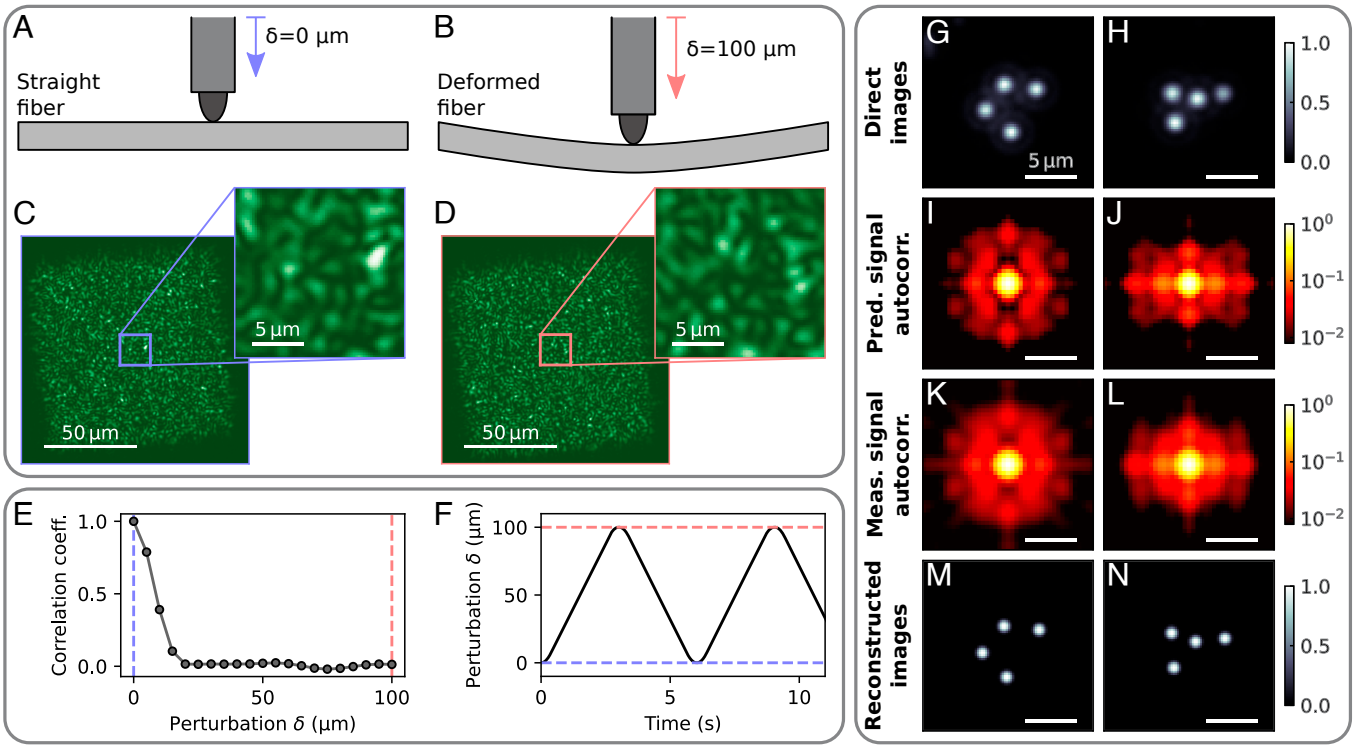

Fig. 4. Reconstructed images of fluorescent beads through a dynamically perturbed square-core fiber. (*A* and *B*) Sketch of the deformation procedure used to dynamically perturb a 10.5-cm-long fiber (sketch not to scale). (*C* and *D*) Transmitted speckle patterns for $\delta = 0$ μm (straight fiber) and $\delta = 100$ μm (deformed fiber), demonstrating that the applied perturbation leads to a decorrelation of the transmitted field. (*E*) Correlation coefficient as a function of the applied perturbation, taking as a reference the speckle pattern measured for $\delta = 0$ μm. (*F*) Temporal dependence of the perturbation applied to the fiber during the experiments. This periodic perturbation is applied during the full acquisition time (approximately 4 h). (*G* and *H*) Direct fluorescence images of objects composed of fluorescent beads located at the output of the fiber. (*I* and *J*) Predicted signal autocorrelations calculated with the true position of the beads using Eq. **2**. (*K* and *L*) Signal autocorrelations retrieved from experimental measurements (averaged over $N_{\text{rep}} = 40{,}000$ speckle illuminations). (*M* and *N*) Reconstructed images of the beads. Despite the dynamic perturbation applied to the fiber, the position of the beads is accurately retrieved.

related artifacts, the quality of reconstructed images is already relatively good with 3,000 realizations (*SI Appendix*, section S5). Furthermore, it might be envisioned that better reconstruction algorithms (e.g., based on artificial neural networks) could be used to reduce the influence of statistical fluctuations on the quality of the reconstructed images.

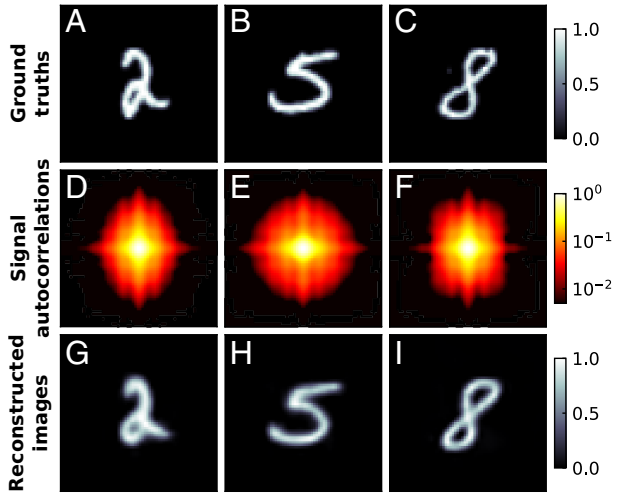

Fig. 5. Reconstructed images of handwritten digits in numerical simulations. (*A*–*C*) Grayscale images from the MNIST database of handwritten digits (42), that are used as objects in our numerical simulations. (*D*–*F*) Signal autocorrelations of these objects calculated using Eq. **2**. (*G*–*I*) Images reconstructed by an artificial neural network, demonstrating that the inverse problem underlying our approach can be successfully solved even in the case of continuous objects.

Different strategies can also be envisioned in order to tackle limitations imposed by the restricted field of view. In our experiments, we created a single area of interest by photobleaching all other beads within the field of view of the fiber. However, if the fiber can collect light from several objects of interests that are not in the range of the memory effect, the resulting signal autocorrelation is the (incoherent) sum of the signal autocorrelations associated with each object. In this case, it might then be possible to unscramble these contributions and retrieve an image of each object, even though the relative position between these objects would remain unknown. An alternative option would be to deposit an opaque coating at the fiber output in order to reduce the field of view of the fiber down to the area covered by the memory effect. In parallel, there exist several opportunities to extend the field of view of the approach, in the perspective of studying larger objects. A possible way to extend the field of view consists in increasing the range of the memory effect by optimizing the optical properties of the fiber so that boundary conditions at the core-cladding interface are closer to those of a perfect mirror. It might also be possible to combine the spatial information available via the kaleidoscopic memory effect with the deterministic information provided by the knowledge of the eigenbasis of the fiber (12) in order to extend the field of view. Finally, our approach could also benefit from the use of matrix factorization algorithms, not only to reconstruct images beyond the range of the memory effect (18) but also to probe the dynamics of fluorescent objects (43).

Conclusion

To conclude, we introduced an approach to reconstruct images through a multimode optical fiber based on speckle correlations without any prior information on the fiber. This approach takes advantage of symmetries in square-core fibers, which induce a kaleidoscopic memory effect that can be exploited to reconstruct images through the fiber. As an illustration, we reconstructed images of samples composed of several fluorescent beads, as being relevant, e.g., for applications involving fluorescent emitters as functional indicators (44, 45). Moreover, we demonstrated that our approach is robust to dynamic fiber perturbations. Finally, using numerical simulations, we evidenced that the inverse problem underlying the approach can be successfully solved even in the case of more complex objects. We anticipate that better strategies to solve this inverse problem will emerge from the recently established fields of compressed sensing (46) and deep learning (47), e.g., by reducing the influence of statistical fluctuations and by finding adequate sparsity constraints. Furthermore, we highlight that our method is generally applicable not only to fluorescent objects but also to any sample that generates a signal in response to light, such as photoacoustic emission from optical absorbers (48–50) or second-harmonic generation from nonlinear materials (51, 52).

Materials and Methods

Sample Preparation. Fluorescent objects are composed of latex microspheres (ThermoFisher Scientific, red FluoSpheres, diameter 1.0 μm) dispersed on a glass coverslip. A solution of Poly-L-lysine (Sigma-Aldrich, 0.1 % in H_2O) is first deposited on a clean coverslip in order to fix the microspheres. A solution of fluorescent beads diluted in water is then deposited on the coverslip. Using this procedure, fluorescent beads are randomly dispersed on the sample. In order to detect only the fluorescence of the few beads of interest, we selectively photobleach all other beads within the field of view of the fiber (area of 100 μm × 100 μm) by successively focusing coherent light from a continuous-wave laser (Cobolt 08-DPL, 532 nm, 10 mW after attenuation by a neutral density filter) on the beads using a ×20 objective (Mitutoyo Plan Apo SL 20X/0.28).

Experimental Setup. The optical setup that we built to image fluorescent objects through a multimode fiber is represented in *SI Appendix*, section 1. Coherent light is generated by a continuous-wave solid-state laser (Cobolt 08-DPL, 532 nm). Light is injected in a single-mode polarization-maintaining fiber and outcoupled using a collimator (Schäfter+Kirchhoff 60FC-L-4-M75-01). Light then passes through a linear polarizer to ensure that it is horizontally polarized before being reflected by a digital micromirror device (Vialux Superspeed V-7001). Random speckle patterns are generated and translated in the plane of the fiber using Lee holography (53). This technique is implemented using a 4f system composed of a 300-mm lens (L1) and a 150-mm lens (L2). In the focal plane between these lenses, an iris selects the first diffraction order of the grating displayed by the DMD. A dichroic mirror (Chroma ZT532rdc) reflects the light toward a ×20 objective (Nikon CF Plan 20X/0.35 EPI SLWD), and a square-core multimode fiber (CeramOptec, core section 100 μm × 100 μm, cladding diameter 123 μm, numerical aperture 0.22) is placed in its focal plane. The input speckle patterns generated using this procedure are characterized by a numerical aperture of 0.22 (to match that of the fiber) and a spatial extent of 92 μm × 92 μm. This allows us to translate the patterns over an area of 8 μm × 8 μm without illuminating the fiber cladding. Note that to avoid autofluorescence of the fiber coating, we removed it using a solution of trichloromethane.

The sample, located approximately 20 μm away from the fiber output, is thus illuminated by light coming from the fiber. Fluorescence light is then collected by the same fiber, and after passing through the dichroic mirror, it is spatially filtered using a 4f system composed of a 200-mm lens (L3) and a 100-mm lens (L4), with an iris located in the focal plane in-between these lenses. This iris is used to block unwanted light coming from outside of the fiber core. Light is then spectrally filtered using two successive fluorescence filters (Thorlabs NF533-17 and Chroma ET577LP) and focused using a 150-mm lens onto a photomultiplier tube module (Hamamatsu H7422P). The measured analog signal passes a low-noise current amplifier (Stanford Research Systems SR570), which applies a low-pass filter to the signal (−6 dB cutoff frequency: 10 kHz) in order to improve the signal-to-noise ratio. Finally, this analog signal is converted into a digital signal by an acquisition board (National Instruments PCIe-6321).

Dynamic deformations are applied to the fiber by holding the fiber at both extremities and by pushing it at midlength using a small rod (diameter 2 mm), along the y direction (corresponding to the vertical direction in our experiments). The position of the rod is controlled using a motorized stage (PI M-230.25) connected to a different computer, ensuring that measurements and perturbations are performed in an asynchronous manner.

Acquisition Procedure. To minimize the acquisition time, we first precalculate the patterns that will be displayed by the DMD. These patterns are split into packets of 79 realizations of input speckles, each containing 21 × 21 patterns which are translated versions of the same speckle. These files are then stored on a solid-state drive (SSD) in a binary format. During an acquisition, each file is loaded on the random access memory (RAM) of the computer (loading time, 2.4 s), transferred into the internal memory of the DMD (transfer time, 8.7 s), and finally displayed by the DMD running at a rate of 2 kHz (display time, 17.4 s). Thus, overall, measuring data for 40,000 realizations takes approximately 4 h. Note that while our DMD could be operated at a rate of up to 23 kHz, working at 2 kHz allows us to improve the signal-to-noise ratio by applying a low-pass filter (−6 dB cutoff frequency: 10 kHz) to the measured signal. Finally, to obtain direct images of the sample, we used a ×20 objective (Mitutoyo Plan Apo SL 20X/0.28) located on the other side of the sample, along with a 200-mm lens, a fluorescence filter (Chroma ET590/50m), and a complementary metal oxide semiconductor (CMOS) camera (Basler acA1300-200um). Direct images were then obtained by averaging the measured images over random illumination patterns coming from the fiber.

Numerical Simulations. In the numerical simulations, we use as objects 28 × 28 grayscale images from the MNIST database of handwritten digits (42). For consistency with experimental measurements of the intensity correlation function $C_I(\Delta \boldsymbol{r}_a, \Delta \boldsymbol{r}_b)$, these images are rescaled to produce 64 × 64 images, using a magnification factor so that the thickness of the lines forming the digits approximately matches the apparent width of a speckle grain. Hence, in physical units, the field of view of the images presented in Fig. 5 would be 16.4 μm × 16.4 μm (which is the actual field of view of the images presented in Fig. 3). We then numerically calculate the signal autocorrelations for each object using Eq. **2**, using for the intensity correlation function the one measured on the 3-cm-long fiber (*SI Appendix*, section 3). Finally, signal autocorrelations are resampled to produced 64 × 64 images, which will be used at the input of the artificial neural network.

The deep learning model used for image reconstruction is a UNeXt (41), which is a modified version of the U-Net (54) and the ResUNet (55) architectures. Thus, our convolutional neural network is composed of two symmetric networks, an encoder and a decoder, each composed of four convolutional blocks. The encoder extracts complex features to produce a representation of the input in a latent space, while the decoder produces output images with the same resolution as input ones. Context information is propagated from the encoder to the decoder through four skip connections (one for each convolutional block), which provide local information to the global information. As a specificity of the UNeXt architecture, our neural network also includes a convolutional multilayer perception block in order to produce a better representation of the data. We train this neural network via a conventional scheme, using the Adam optimizer, a mean-squared-error loss function, a batch size of 32, and an early stopping procedure. We use the 60,000 examples of the MNIST database as follows: 55,800 examples for training, 3,000 examples for validation, and 1,200 examples for testing. Finally, the performances of the network are assessed using the average structural similarity (SSIM), which allows one to compare the visual similarity between two images.

For classification, we used a DenseNet (40), a convolutional neural network with short connections between layers inside each convolutional block. Each layer obtains additional inputs from all preceding layers and passes on its own feature maps to all subsequent layers. Our DenseNet is composed of three dense convolutional blocks, each of them composed of six layers. We train this neural network via a conventional scheme, using the Adam optimizer, a cross-entropy loss function, a batch size of 32, and an early stopping procedure. As for the UNeXt, we use the same 55,800 examples for training, 3,000 examples for validation, and 1,200 examples for testing.

Data, Materials, and Software Availability. Raw experimental data and Python scripts are available for this article (DOI: https://doi.org/10.57745/B6PSX0) (56).

ACKNOWLEDGMENTS. The authors thank M. Balland, A. Carron, A. Goetschy, and S. Mezil for insightful discussions. This work was supported by the H2020 European Research Council (grant 681514-COHERENCE) and by a Marie Skłodowska Curie Individual Fellowship (grant 750420-DARWIN).

1. J. A. Frank, M. J. Antonini, P. Anikeeva, Next-generation interfaces for studying neural function. *Nat. Biotechnol.* **37**, 1013–1023 (2019).
2. A. W. Snyder, J. Love, *Optical Waveguide Theory* (Springer, 2012).
3. R. N. Mahalati, R. Y. Gu, J. M. Kahn, Resolution limits for imaging through multi-mode fiber. *Opt. Express* **21**, 1656–1668 (2013).
4. H. Cao, A. P. Mosk, S. Rotter, Shaping the propagation of light in complex media. *Nat. Phys.* **18**, 994–1007 (2022).
5. M. A. Bolshtyansky, B. Y. Zel'dovich, Transmission of the image signal with the use of a multimode fiber. *Opt. Commun.* **123**, 629–636 (1996).
6. T. Čižmár, K. Dholakia, Exploiting multimode waveguides for pure fibre-based imaging. *Nat. Commun.* **3**, 1027 (2012).
7. Y. Choi *et al*., Scanner-free and wide-field endoscopic imaging by using a single multimode optical fiber. *Phys. Rev. Lett.* **109**, 203901 (2012).
8. I. N. Papadopoulos, S. Farahi, C. Moser, D. Psaltis, High-resolution, lensless endoscope based on digital scanning through a multimode optical fiber. *Biomed. Opt. Express* **4**, 260–270 (2013).
9. A. M. Caravaca-Aguirre, R. Piestun, Single multimode fiber endoscope. *Opt. Express* **25**, 1656–1665 (2017).
10. L. V. Amitonova, J. F. de Boer, Endo-microscopy beyond the Abbe and Nyquist limits. *Light Sci. Appl.* **9**, 81 (2020).
11. M. W. Matthès, Y. Bromberg, J. de Rosny, S. M. Popoff, Learning and avoiding disorder in multimode fibers. *Phys. Rev. X* **11**, 021060 (2021).
12. M. Plöschner, T. Tyc, T. Čižmár, Seeing through chaos in multimode fibres. *Nat. Photonics* **9**, 529–535 (2015).
13. D. E. Boonzajer Flaes *et al*., Robustness of light-transport processes to bending deformations in graded-index multimode waveguides. *Phys. Rev. Lett.* **120**, 233901 (2018).
14. J. Bertolotti *et al*., Non-invasive imaging through opaque scattering layers. *Nature* **491**, 232–234 (2012).
15. O. Katz, P. Heidmann, M. Fink, S. Gigan, Non-invasive single-shot imaging through scattering layers and around corners via speckle correlations. *Nat. Photonics* **8**, 784–790 (2014).
16. O. Salhov, G. Weinberg, O. Katz, Depth-resolved speckle-correlations imaging through scattering layers via coherence gating. *Opt. Lett.* **43**, 5528–5531 (2018).
17. D. Wang, S. K. Sahoo, X. Zhu, G. Adamo, C. Dang, Non-invasive super-resolution imaging through dynamic scattering media. *Nat. Commun.* **12**, 3150 (2021).
18. L. Zhu *et al*., Large field-of-view non-invasive imaging through scattering layers using fluctuating random illumination. *Nat. Commun.* **13**, 1447 (2022).
19. S. Feng, C. Kane, P. A. Lee, A. D. Stone, Correlations and fluctuations of coherent wave transmission through disordered media. *Phys. Rev. Lett.* **61**, 834–837 (1988).
20. I. Freund, M. Rosenbluh, S. Feng, Memory effects in propagation of optical waves through disordered media. *Phys. Rev. Lett.* **61**, 2328–2331 (1988).
21. S. Schott, J. Bertolotti, J. F. Léger, L. Bourdieu, S. Gigan, Characterization of the angular memory effect of scattered light in biological tissues. *Opt. Express* **23**, 13505–13516 (2015).
22. B. Judkewitz, R. Horstmeyer, I. M. Vellekoop, I. N. Papadopoulos, C. Yang, Translation correlations in anisotropically scattering media. *Nat. Phys.* **11**, 684–689 (2015).
23. G. Osnabrugge, R. Horstmeyer, I. N. Papadopoulos, B. Judkewitz, I. M. Vellekoop, Generalized optical memory effect. *Optica* **4**, 886–892 (2017).
24. H. Yılmaz *et al*., Angular memory effect of transmission eigenchannels. *Phys. Rev. Lett.* **123**, 203901 (2019).
25. L. V. Amitonova, A. P. Mosk, P. W. H. Pinkse, Rotational memory effect of a multimode fiber. *Opt. Express* **23**, 20569–20575 (2015).
26. W. Xiong, C. W. Hsu, H. Cao, Long-range spatio-temporal correlations in multimode fibers for pulse delivery. *Nat. Commun.* **10**, 2973 (2019).
27. S. Li, S. A. R. Horsley, T. Tyc, T. Čižmár, D. B. Phillips, Memory effect assisted imaging through multimode optical fibres. *Nat. Commun.* **12**, 3751 (2021).
28. N. Borhani, E. Kakkava, C. Moser, D. Psaltis, Learning to see through multimode fibers. *Optica* **5**, 960–966 (2018).
29. B. Rahmani, D. Loterie, G. Konstantinou, D. Psaltis, C. Moser, Multimode optical fiber transmission with a deep learning network. *Light Sci. Appl.* **7**, 69 (2018).
30. P. Fan, T. Zhao, L. Su, Deep learning the high variability and randomness inside multimode fibers. *Opt. Express* **27**, 20241–20258 (2019).
31. S. Resisi, S. M. Popoff, Y. Bromberg, Image transmission through a dynamically perturbed multimode fiber by deep learning. *Laser Photonics Rev.* **15**, 2000553 (2021).
32. E. R. Andresen, S. Sivankutty, V. Tsvirkun, G. Bouwmans, H. Rigneault, Ultrathin endoscopes based on multicore fibers and adaptive optics: A status review and perspectives. *J. Biomed. Opt.* **21**, 121506 (2016).
33. T. Yeminy, O. Katz, Guidestar-free image-guided wavefront shaping. *Sci. Adv.* **7**, eabf5364 (2021).
34. R. Kuschmierz, E. Scharf, D. F. Ortegón-González, T. Glosemeyer, J. W. Czarske, Ultra-thin 3D lensless fiber endoscopy using diffractive optical elements and deep neural networks. *Light: Adv. Manuf.* **2**, 415–424 (2021).
35. M. C. Velsink, Z. Lyu, P. W. H. Pinkse, L. V. Amitonova, Comparison of round- and square-core fibers for sensing, imaging, and spectroscopy. *Opt. Express* **29**, 6523–6531 (2021).
36. A. M. Caravaca-Aguirre, A. Carron, S. Mezil, I. Wang, E. Bossy, Optical memory effect in square multimode fibers. *Opt. Lett.* **46**, 4924–4927 (2021).
37. J. R. Fienup, Reconstruction of an object from the modulus of its Fourier transform. *Opt. Lett.* **3**, 27–29 (1978).
38. Y. Shechtman *et al*., Phase retrieval with application to optical imaging: A contemporary overview. *IEEE Signal Process. Mag.* **32**, 87–109 (2015).
39. S. Kirkpatrick, C. D. Gelatt, M. P. Vecchi, Optimization by simulated annealing. *Science* **220**, 671–680 (1983).
40. G. Huang, Z. Liu, L. van der Maaten, K. Q. Weinberger, "Densely connected convolutional networks" in *Proceedings of the IEEE Conference on Computer Vision and Pattern Recognition* (2017), pp. 4700–4708.
41. J. M. J. Valanarasu, V. M. Patel, "UNeXt: MLP-based rapid medical image segmentation network" in *Medical Image Computing and Computer Assisted Intervention–MICCAI 2022*, L. Wang, Q. Dou, P. T. Fletcher, S. Speidel, S. Li. Eds. (Lecture Notes in Computer Science, Springer Nature, Cham, Switzerland, 2022), pp. 23–33.
42. Y. Lecun, L. Bottou, Y. Bengio, P. Haffner, Gradient-based learning applied to document recognition. *Proc. IEEE* **86**, 2278–2324 (1998).
43. C. Moretti, S. Gigan, Readout of fluorescence functional signals through highly scattering tissue. *Nat. Photon.* **14**, 361–364 (2020).
44. S. Weisenburger, A. Vaziri, A guide to emerging technologies for large-scale and whole brain optical imaging of neuronal activity. *Annu. Rev. Neurosci.* **41**, 431–452 (2018).
45. S. Turtaev *et al*., High-fidelity multimode fibre-based endoscopy for deep brain in vivo imaging. *Light Sci. Appl.* **7**, 92 (2018).
46. Y. C. Eldar, G. Kutyniok, *Compressed Sensing: Theory and Applications* (Cambridge University Press, 2012).
47. G. Barbastathis, A. Ozcan, G. Situ, On the use of deep learning for computational imaging. *Optica* **6**, 921–943 (2019).
48. L. V. Wang, J. Yao, A practical guide to photoacoustic tomography in the life sciences. *Nat. Methods* **13**, 627–638 (2016).
49. A. M. Caravaca-Aguirre *et al*., Hybrid photoacoustic-fluorescence microendoscopy through a multimode fiber using speckle illumination. *APL Photonics* **4**, 096103 (2019).
50. J. Zhou, J. V. Jokerst, Photoacoustic imaging with fiber optic technology: A review. *Photoacoustics* **20**, 100211 (2020).
51. P. Campagnola, C. Y. Dong, Second harmonic generation microscopy: Principles and applications to disease diagnosis. *Laser Photonics Rev.* **5**, 13–26 (2011).
52. A. Cifuentes *et al*., Polarization-resolved second-harmonic generation imaging through a multimode fiber. *Optica* **8**, 1065–1074 (2021).
53. W. H. Lee, Binary synthetic holograms. *Appl. Opt.* **13**, 1677–1682 (1974).
54. O. Ronneberger, P. Fischer, T. Brox, "U-Net: Convolutional networks for biomedical image segmentation" in *Medical Image Computing and Computer-Assisted Intervention–MICCAI 2015*, N. Navab, J. Hornegger, W. M. Wells, A. F. Frangi, Eds. (Lecture Notes in Computer Science, Springer International Publishing, Cham, Switzerland, 2015), pp. 234–241.
55. F. I. Diakogiannis, F. Waldner, P. Caccetta, C. Wu, ResUNet-a: A deep learning framework for semantic segmentation of remotely sensed data. *ISPRS J. Photogramm. Remote Sens.* **162**, 94–114 (2020).
56. D. Bouchet *et al*., Experimental data and Python scripts for the article "Speckle-correlation imaging through a kaleidoscopic multimode fiber", Recherche Data Gouv, https://doi.org/10.57745/B6PSX0, Deposited 13 June 2023.